Flow Characteristics of Overexpanded Rocket Nozzles

S.B.Verma
Research Scientist, Experimental Aerodynamics Division,
National Aerospace Laboratories (CSIR), Bangalore - 560 017, INDIA,
Email: sbverma@ead.cmmacs.ernet.in

Oskar Haidn
Head of Technology, DLR Institute of Space Propulsion,
Lampoldshausen, D-74239, GERMANY
Email: oskar.haidn@dlr.de

ABSTRACT

The current paper discusses the exhaust flow features and the various unsteady flow separation characteristics in subscale overexpanded nozzles that lead to generation of side-loads. While a D_iMR type of Mach reflection features in the exhaust of a truncated ideal contour nozzle an I_nMR occurs in a thrust optimized parabolic nozzle. The main contributor towards generation of sideloads in a parabolic nozzle is known to be the flow transitions (free shock separation → restricted shock separation and vice-versa) and the shock unsteadiness preceding them. However, in a truncated ideal contour nozzle (that features only FSS condition) the strongest cause of side-load origin are seen to be (i) the asymmetry of separation front around the nozzle circumference, (ii) length of separation region and, (iii) length of back-flow region. The flow asymmetry causes variations in pressure rise at separation and hence, in the local value of *rms* fluctuations. The length of separation region also shows considerable variations with NPR and tends to peak at NPR similar to those at which peaks in $(\sigma_w/P_w)_{max}$ value and strain-gauge signal occur. Data therefore suggests that that the necessary condition for side-load generation in a TIC nozzle is not just the flow asymmetry but also the length of separation region which shows significant variation as the separation front gradually approaches the nozzle exit. The length of back-flow region, on the other hand, also seems to control the large-scale fluctuations of the separation front. As the extent of back-flow region decreases, the oscillations of separation shock die down with a subsequent drop in the side-load signal even when the separation front exhibits circumferential asymmetry.

LIST OF SYMBOLS

$G(f)$	= power spectral density
f	= sampling frequency, Hz
D_m	= diameter of the Mach disk, mm
L	= length of the divergent section of nozzle, mm
M_{inc}	= Mach number at incipient separation location
P_0	= stagnation chamber pressure, mbar
P_a	= ambient pressure, mbar
P_w	= local mean wall pressure, mbar
P_{pl}	= plateau pressure after separation, mbar
P_{inc}	= incipient wall pressure at separation, mbar
P_{sep}	= wall pressure at physical separation, mbar
R_e	= radius at the nozzle exit, mm
R_j	= radius of the shear-layer at the nozzle exit, mm
r_t	= radius of nozzle throat, mm
X	= co-ordinate along nozzle axis, mm
X_{Dm}	= X-location of the Mach disk from nozzle exit, mm
X_{sep}	= point of physical separation, mm

X_{inc} = point of incipient separation, mm
X_{exit} = X-location of nozzle exit, mm
ϵ_e = area ratio of the nozzle
ϵ_{sep} = area-ratio of nozzle at separation location
σ_w = *rms* of the local wall pressure
$(\sigma_w/P_w)_{max}$ = non-dimensionalized maximum value of *rms* pressure fluctuation
φ = circumferential wall angle, degrees

1. INTRODUCTION

Flow separation in a fluid dynamic system, in general, is a result of a natural adjustment process by which a viscous flow adjusts to its surroundings under particular conditions. This adjustment mechanism may, in certain cases, enhance performance or permit better flow control conditions while in others may result in performance penalties and instabilities that arise from separation. In general, as the flow expands in the divergent section of the nozzle, it separates from the nozzle wall at some axial location where the wall pressure reaches a particular fraction of the ambient pressure [1], Figure 1 (a). This depends upon the nozzle pressure ratio (NPR) and is indicated in the wall pressure distribution by the first rise in wall pressure known as the point of incipient separation, Figure 1 (b). Summerfield criterion [2] predicts that the flow in a nozzle separates when the ratio of wall pressure to the ambient pressure (P_{inc}/P_a) is less than or equal to 0.4. This pressure rise accompanying separation has been found to be a function of the incipient separation Mach number, M_{inc} [3, 4]. Thereafter, the separation region or in other words the region of initial compression terminates at the point of physical separation, Figure 1. This is immediately followed by a "back-flow" or mixing region wherein the separated nozzle flow mixes with entrained air from the atmosphere [3]. Although the major pressure rise occurs in the separation region the remaining increase (which is only a small percentage of the initial rise) occurs in the back-flow/mixing region, Figure 1 (b). It has been reported [3] that the pressure rise occurring in the back-flow/mixing region depends on (i) the entrainment effect of the separated jet and, (ii) on the length and geometry of the nozzle wall downstream of the point of physical separation. In general, the wider is the divergence angle and the shorter the back-flow region the less is pressure in the back-flow region different from ambient pressure. However, this holds good for conical nozzles with divergence angles ≥ 15 degrees [5]. The flow conditions in the back-flow/mixing region of a contoured nozzle, however, are very different from that of a conical nozzle primarily owing to the varying divergence angle of the nozzle wall along its length. This results in lower pressures in the back-flow/mixing region relative to conical nozzles. With increasing NPR the separation point is pushed closer to the nozzle exit and the pressure rise (P_{inc}/P_a) accompanying separation no longer correlates well with the rest of the data. This flow condition is known as the "end-effect" regime wherein the pressure recovery is limited by the reducing length of back-flow/mixing region. Further increase in NPR does not change the separation location but the pressure rise across separation keeps on decreasing with increasing chamber pressure until at very high NPR the wall pressure at nozzle exit becomes equivalent to the ambient pressure (full-expansion).

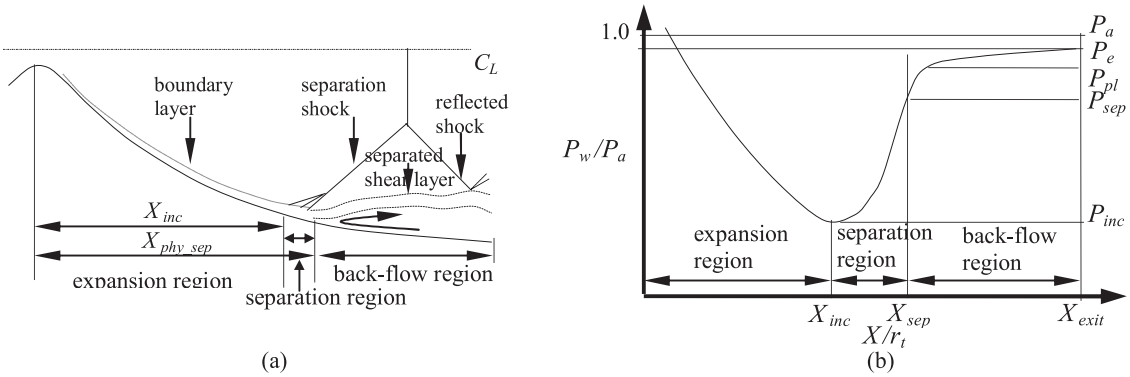

Figure 1. Schematic showing the (a) flow features of an overexpanded nozzle and, (b) wall pressure distribution in an overexpanded nozzle

In an overexpanded convergent-divergent (C-D) nozzle, such flow conditions occur when the nozzle expansion ratio is too large for a given NPR, e.g., when the main stage engine uses a high area-ratio nozzle and is operated under sea-level or low-altitude conditions. Flow separation in such cases becomes inevitable with high risk of side-load generation. These flow conditions are prevalent mostly during impulsive start-up or shut-down of engines under ground testing/lift-off, during stage separation and also during steady engine operation with flow separation inside the nozzle. Side-loads have been observed both in sub-scale and full-scale rocket engine nozzles during such operations. The resulting side-forces, although momentary, can be large in magnitude and are known to cause failures of nozzle exit cone structures and thrust vector control gimbal actuators [6]. However, side-loads may have different origins, such as due to asymmetric separation line, pressure pulsations in the separation region, aeroelastic coupling, flow instability etc. on the basis of which, different models have been developed for their prediction [7]. Most of the earlier nozzle flow studies were initiated by the side-load activity observed by Nave and Coffey [8] during the cold-gas subscale nozzle tests of the J2-S engine (with a parabolic nozzle) in 1973. Recent studies in Europe [9-15] identified a type of side-load behavior that originates as a result of flow transition from free shock separation (FSS) to restricted shock separation (RSS) and *vice-versa*. Their results revealed that the key driver to such flow transitions is the cap-shock pattern which can occur only in nozzles featuring an internal shock (e.g., the thrust optimized parabolic (TOP) and compressed truncated perfect (CTP) nozzles). Intense side-load activity has not only been observed in the rocket nozzles of most high performance launch vehicles using TOP contour (e.g., SSME and Vulcain engine) design and the CTP design (e.g., LE-7A engine used on the Japanese H-IIA launcher) but also in those using truncated ideal contour (TIC) design (e.g., LR-115 (Saturn C-1), Viking (Ariane 4) and RD-0120 engine (Russian Energia Launcher)) that features a Mach disc. For an engine, therefore, that satisfies both low-altitude operation and high-altitude performance, flow separation characteristics have to be thoroughly understood and controlled. This will help predict, more accurately, flow separation which is required in designing new rocket nozzles. As such research activities in Europe, lead by the flow separation control device (FSCD) group [9-16], and in Japan [17,18], by the JAXA nozzle group, have intensified during the recent years in order to enhance the current knowledge on flow separation and the associated side-load activity.

Although numerous investigations of flow separation in contoured nozzles have been made [5- 18], the causes of flow unsteadiness accompanying separation have received little attention and are not completely understood. In fact, very few studies [19-23] report the flow unsteadiness accompanying the flow separation phenomena in such nozzles. This paper discusses the exhaust flow features and the various unsteady flow separation characteristics that lead to side-load generation in overexpanded subscale rocket nozzles. Results reveal that the variation in the length of separation region and back-flow region seems to have a strong relation towards the generation of flow unsteadiness and hence, side-loads. The experimental test campaign was conducted in the subscale cold-flow test facility at DLR Lampoldshausen. Real-time wall pressure measurements using fast piezo-resistive pressure sensors are acquired along two streamwise locations, one at circumferential location of $\varphi = 0^\circ$ and the other at $\varphi = 180^\circ$ to check for any flow asymmetry. Surface oil-pigment visualization method is employed to measure changes in the location of physical separation in response to varying NPR whereas spark schlieren is used to study the exhaust flow patterns.

2. EXPERIMENTAL SETUP AND PROCEDURE

2.1 Test Facility

Tests were carried out in the subscale cold gas test facility enhanced with an additional horizontal test bench, as shown in Figure 2 (a) (see ref. 16 for more details) and not in the high-altitude simulation chamber which limits visibility during test campaigns with surface oil flow, infrared thermometry etc. This facility uses dry nitrogen at ambient temperature as the test gas due to its advantage over compressed air, i.e., the absence of humidity and other impurities that can otherwise cause condensation of flow during operation. The nozzle pressure ratio was adjusted by varying the nozzle feeding pressure, P_0, and under present test limitations with the nozzle blowing into atmospheric pressure maximum pressure ratio up to 60 could be achieved. The throat diameter of the sub-scale TIC nozzle used for the experimental investigation was 20mm, yielding maximum mass flows in the range of m = 4.2 kg/sec. Comparisons are also made with the results of the TOP nozzle (similar throat diameter) wherever necessary. Both the TIC and TOP nozzles are of identical mass and designed to give identical specific impulse in vacuum and nozzle exit pressures, P_e [4]. The only substantial difference therefore

between the two nozzles is their side-load activity. The area-ratio (ϵ_e) of the TIC and TOP nozzle is 20.66 and 30, respectively.

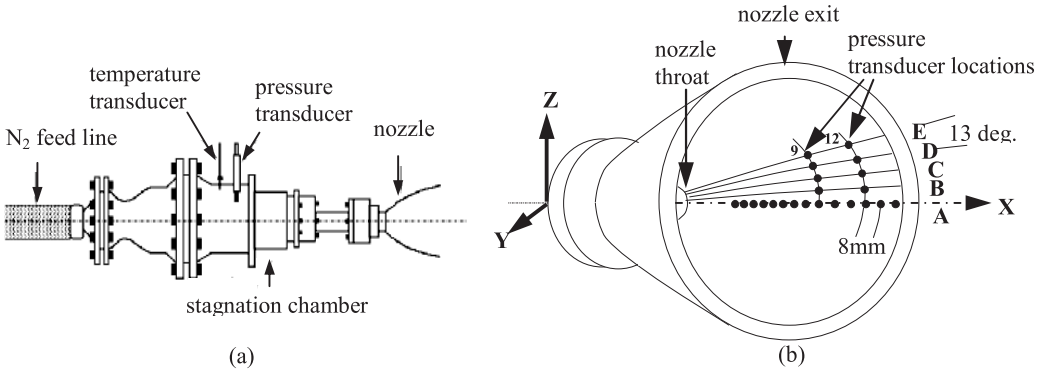

Figure 2. (a) Schematic of the cold gas subscale nozzle test-facility and (b) schematic of the pressure sensor locations and the choice of axis on a TIC nozzle

2.2 Wall Pressure Sensors and Data Acquisition

Wall pressures both upstream and downstream of the throat are measured using fast piezo-resistive pressure sensors (Kulite Semiconductor Inc. model XT-154-190M). These transducers have a pressure-sensitive area of 0.71mm in diameter and an outer case diameter of 3.9mm. According to the manufacturer's specifications, these transducers have a natural frequency of 50kHz and are capable of operating in the temperature range of – 40˚C to + 85˚C and 0 to 100% relative humidity. The accuracy, according to manufacturer's specification is within 0.5% in the operating pressure range of 0-15psia. The sensitivity of the transducers is typically 97.206mV/bar. All the transducers were calibrated statically against atmospheric pressure. Four such pressure sensors are placed in the stagnation chamber and 14 along a single axial line in the supersonic section of the TIC nozzle at $\varphi = 0^\circ$ (with a pitch of 8 mm, sampling frequency 1kHz with low-pass filter cut-off frequency of 160Hz). Four transducers were placed circumferentially (placed 13 degrees apart) both at the 11th and 12th transducer locations, Figure 2 (b). The sampling frequency for these transducers was 25 kHz with low-pass filter cut-off frequency of 8kHz. In order to capture any flow asymmetry, pressure points were also fabricated in streamwise direction at circumferentially opposite locations, i.e. at $\varphi = 180^\circ$, for locations 5 to 12 at $\varphi = 0^\circ$.

Surface flow patterns were visualized using the classic oil pigment mixture (using vacuum pump oil, titanium dioxide and oelic acid) to capture variations in the location of physical separation to changes in NPR. Online recording of visualization tests was done with a camera looking up into the nozzle which was later digitized to extract vital flow information. Contrary to usual side load measurement devices, where forces perpendicular to the nozzle axis are determined by measuring the resulting torque with respect to a cardan point, the P6.2 test stand uses, inspired by Dumnov [7], a simple, very thin-walled bending tube, made of a special aluminium-alloy is mounted upstream the convergent nozzle part (Figure 2). It resists the high nozzle feeding pressure, but is still sensitive to lateral forces. Pairs of two strain gauges are applied in each quadrant. Opposite pairs build a full Wheatstone bridge to measure one of the two lateral directions. Due to the wiring only bending strains are measured. All other strains, provoked by the inside pressure, the longitudinal nozzle force and temperature effects, are compensated. The first eigen frequency of the bending tube calibrated under static tests was found to be 73.245Hz.

3.0 RESULTS AND DISCUSSIONS

Convergent-divergent nozzles are designed to generate high Mach number flows for a given chamber pressure and area-ratio. Initially for rockets, conical nozzles were being used which performed well as long as the nozzle half angle was kept between 12 and 18 degrees. However the pressing needs for higher thrust required high area-ratio nozzles to be used but with minimum nozzle exit divergence losses. Keeping the divergence loss low, in a high area-ratio nozzle, results in a long nozzle that has a penalty in the rocket propulsion system mass. This problem was solved by using bell-shaped nozzle that

is designed to expand the high pressure chamber gases more efficiently than the conical nozzle of same area-ratio and length. However, the flow inside such nozzles is primarily determined by the wall contour angle downstream of the last point of the circular arc forming the nozzle throat, see Figure 3 [ref.1]. The demand for higher thrust requirements therefore resulted in contoured nozzles that have wall angles ranging between 16 degrees to as high as 38 degrees, Figure 3 (a). In parabolic nozzles, the contour downstream of the circular arc forming the throat is not adapted to the expansion waves coming from the throat (unlike the ideal nozzle design). At this transition point, the wall contour and wall slope are both continuous while the wall curvature is discontinuous [24]. As a result compression waves are induced by the parabola leading to formation of an internal shock (IS), Figure 4 (b). A cap-shock pattern, typical to such nozzles, results from an interaction of the over-expansion or the separation shock (coming from the nozzle wall) and an inverse Mach reflection of the internal shock at the nozzle centerline. It can be seen in Figure 3 (b) that the change in contour for the truncated ideal contour nozzle is not as severe as seen for TOP nozzle. This results in significant changes in the structure of exhaust flow development in each case, Figure 4 (a).

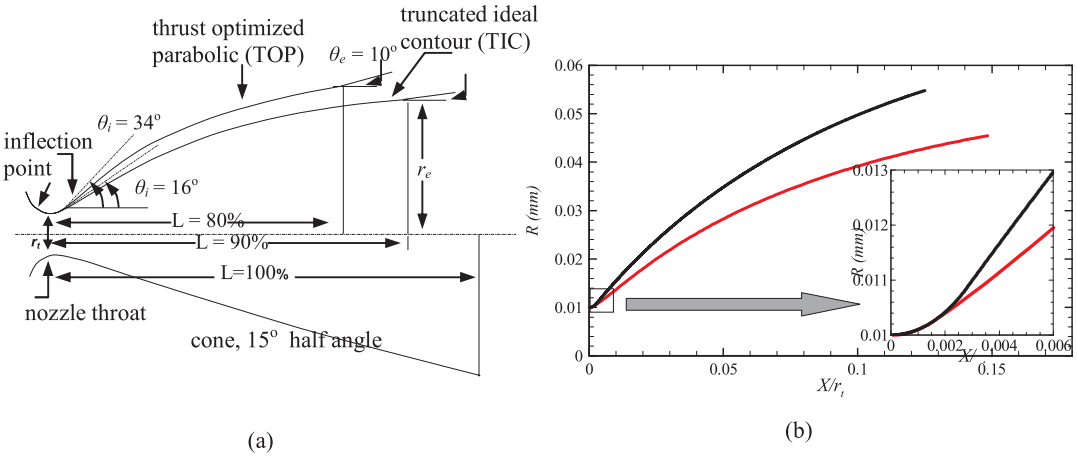

Figure 3. Schematic showing the variation in divergence angles downstream of the point of circular arc forming the throat, for different nozzles used in rocket engines ref. [6].

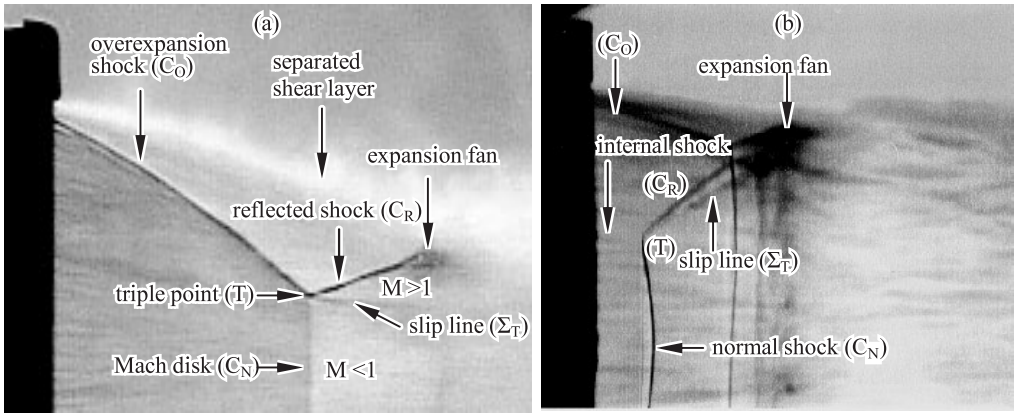

Figure 4. Schlieren pictures showing the exhaust flow features of an overexpanded (a) TIC nozzle and, (b) TOP nozzle; NPR=60

3.1 Exhaust Flow Features

Mach Reflections

Courant and Friedrichs in 1948 [25] while investigating the shock reflection phenomena indicated the existence of three types of Mach reflections (MR) broadly classified on the basis of the slipstream direction from the triple point location. According to them if the slipstream from the triple point moves away from the reflected shock, the Mach reflection is called direct Mach reflection (D_iMR), if it moves

parallel to exhaust centerline, it is called stationary Mach reflection (S_tMR) and finally if it moves towards the reflected shock, it is called the inverse Mach reflection (I_nMR). The first and the last cases are encountered in the flows discussed in the following sections.

3.1.1 Direct Mach Reflection (D_iMR)

The type of Mach reflection that is observed in the TIC nozzle is the direct Mach reflection (D_iMR) or the type-II shock/shock interference, Figure 4 (a). The type-II interference situation arises when the strengths of separation/overexpansion shocks (C_O) are high enough so that the crossing of these shocks along the centerline is replaced by a nearly normal shock, or Mach disk, between the triple points (T) [26]. The separation caused on the lower and upper walls gives rise to a lambda shock pattern, with the flow behind the separation shocks (C_O) being still supersonic. The reflected shocks (C_R) form the legs of the lambda shock.

The flow while passing through set of successive shocks (C_O) and (C_R) experiences an entropy rise that is different from that it undergoes while passing through the Mach disk alone. As a result a slip line ($\sum_T$) separates the downstream flows from normal shock or Mach disk (C_N) and the one passing through oblique shock (C_R), which have different velocities, densities, temperatures, Mach numbers but identical pressures. The subsonic channel downstream of the Mach disk and bound by the slip line, is accelerated under the influence of adjacent flows, so that sonic throat appears after which the flow is again accelerated to supersonic speeds [26]. The penetration of the reflected shock wave (C_R) in the separated shear layer generates a reflected expansion fan (that deflects the shear layer away) which on reflection from the slip line ($\sum_T$) forms a converging fan of compression waves that coalesces downstream to form a single compression wave (that turns the separated shear layer towards the centerline flow direction). For an axisymmetric case, the triple points are replaced by a "circular triple line'' and the slipline by a cylindrical one.

3.1.2 Inverse Mach Reflection (I_nMR)

The exhaust flow pattern from thrust optimized parabolic (TOP) and compressed truncated ideal contour (CTIC) nozzle is significantly different from what is observed from a TIC or conical nozzle. In these nozzles the internal shock (C_I) terminates in a normal shock near the centerline with a cap-shock or reflected shock (C_R) emanating from the triple point. This pattern resembles a Mach reflection in the sense that here the cap-shock (C_R) can, in fact, be thought of as a Mach reflection of the internal shock (incident shock (C_I)). However, a major difference exists relative to D_iMR case and that lies in the orientation of the slipstream. Whereas in D_iMR, the slipstream extends from the triple point towards the exhaust centerline, in an I_nMR the slipstream extends away from the centerline along the reflected shock (C_R), as shown in Figure 4 (b). I_nMR is generally considered as a temporary reflection phenomena [26] and terminates when the triple point collapses along the centerline as the internal shock proceeds towards transitional regular reflection (TRR) [26]. The main part of TRR is the RR wave configuration followed by a new triple point and an additional shock wave that emanates from the new triple point perpendicular to the centerline [26]. The physical reason for the formation of an additional shock wave in TRR (new Mach disk) is to compensate for the sudden drop in pressure that is associated with this transition [27].

So with increase in NPR, the normal shock is pushed downstream with a consequent reduction in its lateral extent (because the lateral extent of high Mach number flow bounded by internal shock in the vicinity of the centerline gradually decreases [28], Figure 5 (a)) until at some downstream location the internal shock converges and intersects the centerline, Figure 5 (b). When this happens the exhaust flow pattern experiences a major change with a flow transition from cap-shock to a Mach disk, as seen in the hot-firing test pictures of SSME, Figure 6. This marks the transition from $I_nMR \rightarrow D_iMR$ and happens for a TOP nozzle in high altitude mode or at high NPR, Figure 5 (b). A new triple point forms where the Mach disk intersects the overexpansion shock (CO) that forms a reflected shock (C_R) as in D_iMR. Centerline pressure distribution obtained from computational studies [28] show two pressure jumps, one caused at the cross-over location of internal shock and followed by the other caused by the Mach-disk.

As for any transition, like RR to MR and *vice-versa*, a "hysteresis" exists in this case too. The forward transition from I_nMR to D_iMR is sudden whereas the backward transition occurs gradually since the Mach disk in this case first approaches the intersection point of internal shock to experience the backward transition. Such hysteresis has been observed in the Vulcain engine tests at DLR

[10,16,28]. Further increase in NPR causes the nozzle exit pressure P_e to increase which results in a gradual reduction in the strength of overexpansion shocks and eventually the Mach disk gets replaced by a regular reflection RR (type-I interference). Finally, as the design NPR for the nozzle is approached the overexpansion shock disappears and the nozzle exhaust flow becomes full-flowing and shock-free.

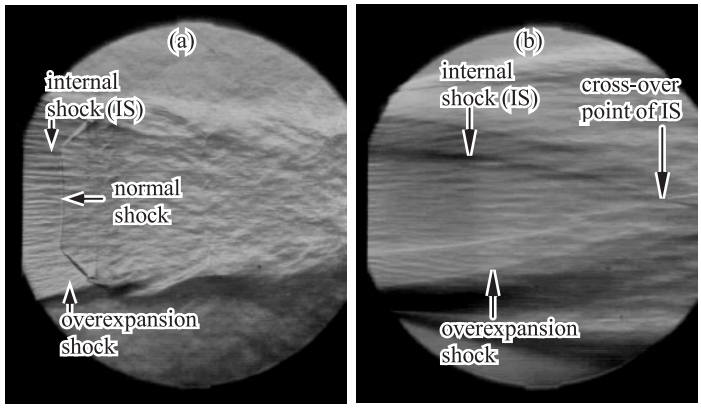

Figure 5. Schlieren pictures showing details of the exhaust flow pattern from a TOP nozzle; (a) NPR=79 and, (b) NPR=610

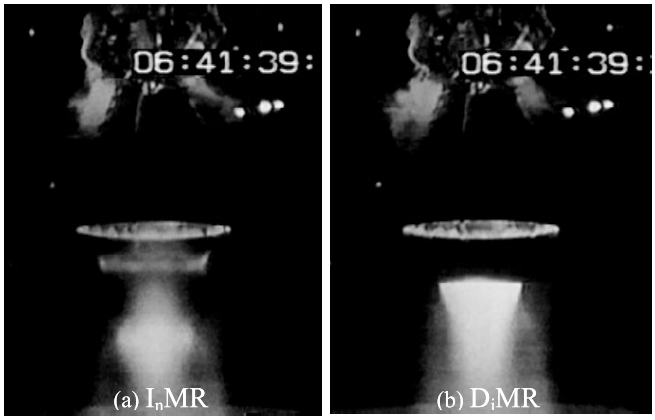

Figure 6. Exhaust flow pattern from SSME showing flow transition from I_nMR to D_iMR at high pressure-ratios

3.1.3 Flow-Field Features of Over-Expanded Nozzles

Typical flow-field features of an overexpanded nozzle are schematically shown in Figure 7 (a). Here the variation in the diameter of the Mach-disk or normal shock (D_m) and its distance from the nozzle exit (X_{Dm}) are measured (from schlieren pictures) for a range of nozzle pressure ratios. It can be seen that the variation in the distance of the Mach-disk (X_{Dm}) with NPR follows a particular trend similar to that followed by sonic jets, Figure 7 (b). This distance increases with increasing NPR until at higher values after which the trend approaches an asymptotic value. Although a similar trend is followed by the normal shock from a TOP nozzle, its location from the nozzle exit is much less than that of the Mach disk from a TIC nozzle. The variation in the diameter of the Mach-disk/normal shock (D_m) with NPR, however, shows some interesting trends, Figure 7 (c). It can be seen that the Mach-disk for the TIC nozzle initially grows in size, reaches a maximum diameter at NPR of approximately 35 after which it begins to decrease with increasing NPR. The decreasing Mack-disk diameter is associated with significant elongation of the first shock-cell length, Figure 7(b). Stark and Wagner [29] recently reported that the axial position of the Mach-disk and its diameter are not affected by the nozzle length or by the varying extent (length and radial-size) of back-flow region. The normal shock in the TOP nozzle also follows a similar trend except that (a) its diameter is much higher than the Mach disk for similar NPR (due to inverse Mach reflection) and, (b) the change in the trend of normal shock size

variation occurs at much higher NPR (of approximately 70), Figure 5 (a) after which it begins to decrease as was observed for the TIC nozzle.

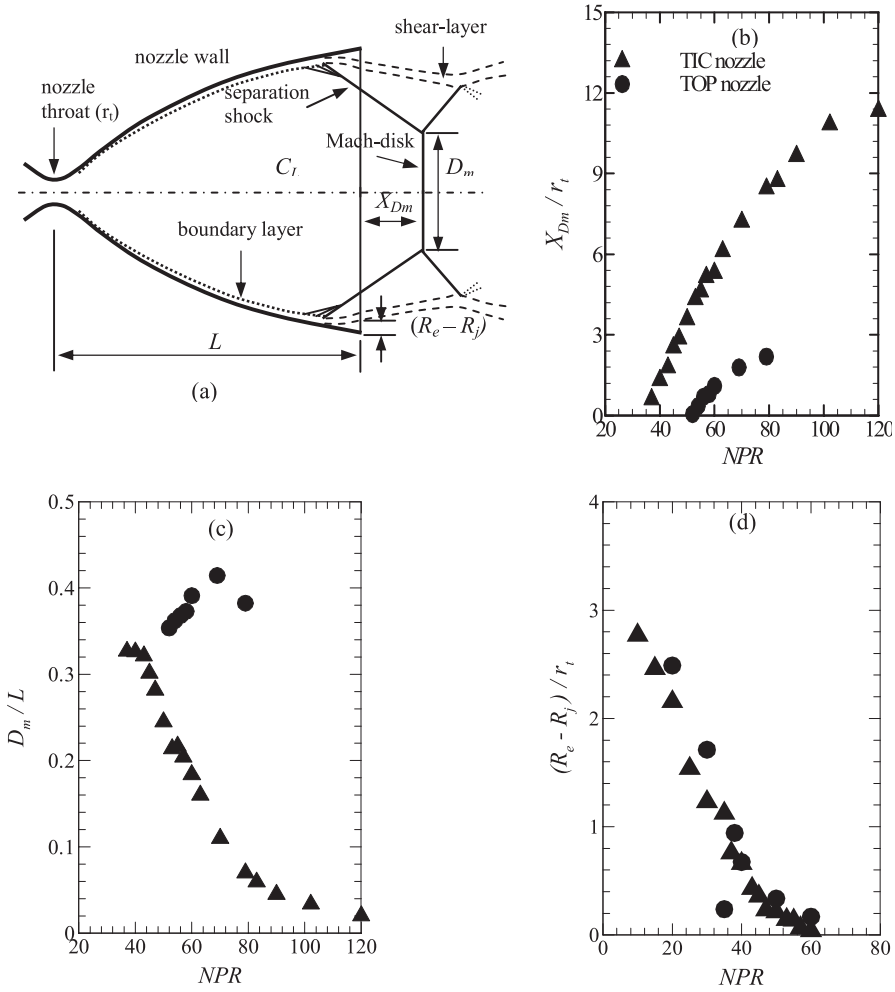

Figure 7. (a) Schematic of the flow-field features of an overexpanded nozzle; Variation of (b) Mach-disk diameter, (c) Mach-disk axial distance and, (d) radius of re-circulation region as a function of NPR, respectively.

At very high NPR the shock structure in the TOP nozzle undergoes a sudden transition from I_nMR to D_iMR and the overexpansion shocks later meet at a point along the centerline. Further increase in NPR makes each nozzle full-flowing and shock-free. The radial size of the recirculation/ back-flow region $(R_e - R_j)/r_t$ also shows a decreasing trend (as expected) with increasing NPR until the separation shock reaches the nozzle exit where it becomes nearly zero, Figure 7 (d). However, for the TOP nozzle a discontinuity in this trend is observed for NPR of 35 after which the previous trend is again followed. This discontinuity is caused by the flow transition from free-shock separation (FSS) to partially formed restricted shock separation (pRSS) which pushes the separation location downstream and gives the appearance to the nozzle exhaust similar to a full-flowing nozzle [30]. During this condition, the exhaust flow fluctuates between FSS and RSS as a function of time and is known to generate high side-loads in this class of nozzle. Once the partially formed separation bubble (as a consequence of pRSS) reaches the nozzle exit, it opens up causing the ambient air to rush in thereby pushing the separation front upstream. When this happens, the $(R_e - R_j)/r_t$ value shows a sudden increase and the previously followed trend continues.

The separation characteristics in a TOP nozzle that lead towards the generation of side-load activity have been discussed in detail is ref. [21, 22] and so will not be repeated here. Therefore, the separation characteristics of TIC nozzle alone will be discussed in this paper.

3.2 Separation Characteristics of a TIC Nozzle

3.2.1 Streamwise Wall Pressure Distributions

Figure 8 (a) shows the streamwise mean wall pressure distribution for a start up sequence. Here the wall pressure P_w is non-dimensionalized by the ambient pressure P_a, and the nozzle axial distance X is non-dimensionalized by the nozzle throat radius, r_t. It can be seen that as the flow accelerates, it expands until at some downstream location where it experiences a sudden jump in wall pressure indicating the point of incipient separation. Thereafter, a gradual pressure adaptation to the ambient pressure occurs over the remaining length of the nozzle. The pressure in this region was generally observed to remain in the range of 0.8 to 0.95. This region is the backflow region wherein the pressure drop occurs due to acceleration of ambient air caused by the pumping action of the separated mixing-layer. For NPR : 40, the incipient separation location moves closer to the nozzle exit with an accompanying reduction in length of the back-flow region and a decrease in pressure adaptation. This marks the beginning of separation "end-effect" as shown in Figure 8 (b) where a change in trend for separation pressure ratio (P_{inc}/P_a) is clearly apparent. It can be seen that the P_{inc}/P_a value initially decreases with increasing NPR but later on starts to increase for NPR ≥ 40 as X_{inc} reaches 80% of the area-ratio (ϵ_e) [16]. This is because for M_{inc} to remain constant for a constant Mach number area-ratio nozzle, increasing *P0* will result in an increase in P_{inc} to maintain this Mach number. Increase in P_{inc}, on the other hand reduces the strength of the compression shock (P_a being constant) resulting in a decrease in its deflection angle. An immediate outcome of this is an increase in the length of the 1st shock cell, seen in Figure 7 (b). Further increase in P_0 will gradually make $P_e = P_a$ which makes the nozzle full-flowing and gives a uniform distribution of M_{inc} at the nozzle exit.

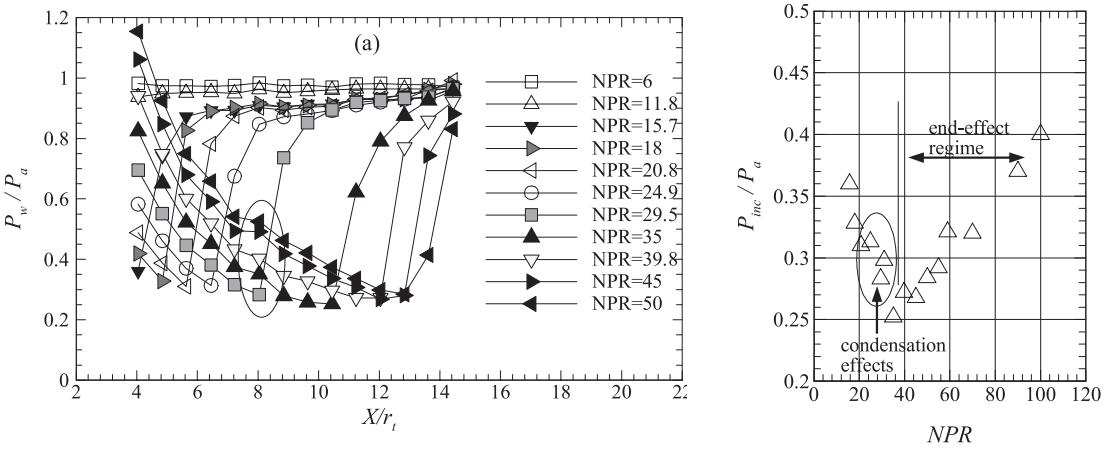

Figure 8. (a) Streamwise distribution of normalized mean wall pressure as a function of nozzle pressure ratio; start up sequence (b) separation pressure ratio distribution showing the two flow regimes prevalent in overexpanded nozzles

No unusual behavior is indicated in the mean pressure distribution except that for NPR > 24.9, a larger than usual downstream movement in separation locations is observed. With each increase in NPR value by 5, the axial movement of X_{inc} (identified by the lowest wall pressure in each pressure plot) increases by 2 pressure locations and then reaches a maximum (3 pressure points) between NPR=30 and 35. Thereafter, X_{inc} movement once again reduces to 2 pressure points and finally by one point as nozzle exit is approached. Additionally a small increase in wall static pressure (seen as a bump and marked by an ellipse in Figure 8) at X/r_t =7.845 for NPR>30 is observed. This is caused due to the onset of nitrogen gas condensation at this axial position [29]. It is well known that this increase in pressure is caused by the release of latent heat due to condensation [31]. As a result a reduction of Mach number in front of the compression shock occurs. This delays separation in order to maintain the dependence of the shock location with Mach number [32-33]. This effect is seen also in Figure 8 (a) for NPR between 29 and 31 and also seen clearly in Figure 8 (b) with the data points not following the general trend. The compression waves generated by condensation later develop into a condensation shock making it easily visible to the naked eye.

3.3 Causes of Side-Load Origin

The origin of side-loads in a TIC nozzle is generally attributed to the following causes:

3.3.1 Flow Asymmetry

One of the strongest causes of lateral force origin nozzles is the asymmetry of separation front around the nozzle circumference. The origin for this flow asymmetry is not fully understood and a lot of experimental and computational effort is being put to investigate the phenomena. An immediate effect of this, however, is the variation in pressure rise at separation (circumferentially) and hence in the local '*rms*' value *which is very sensitive to the extent of separation region* (this in turn may also be sensitive to the variations in local wall contour). In order to investigate the flow asymmetry, 8 pressure points were fabricated at circumferentially opposite locations at $\varphi = 180^\circ$ (for locations 5 to 12 at $\varphi = 0^\circ$). Data was simultaneously acquired from transducers located both at $\varphi = 0^\circ$ and 180° for a number of tests. Figures 9 (a) and (b) show the streamwise mean wall pressure distribution and its corresponding *rms* distribution for one such case with NPR held constant at 28.9 for approximately 8 seconds. A significant asymmetry can be seen for the incipient separation location and in the pressure adaptation to ambient pressure in the back-flow region, thereafter.

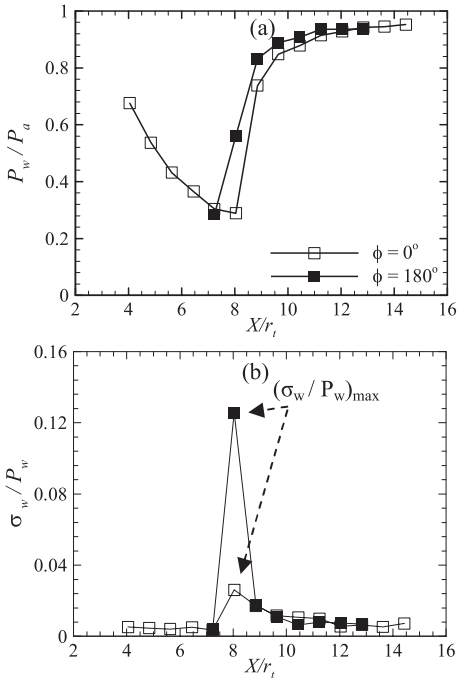

Figure 9. Streamwise distribution of (a) normalized wall pressure and, (b) normalized *rms*; NPR=28.9 (start up sequence)

It is well known that a moving shock generates an intermittent wall pressure signal and results in a sharp rise in fluctuation intensity at separation, represented for example, by the standard deviation of the wall pressure signal [34]. A large increase in σ_w indicates the intermittent nature of the pressure fluctuations caused by the back and forth motion of the separation shock [34] and a peak in its value as an indication of degree of unsteadiness [35]. The *rms* distribution, Figure 9 (b), shows a peak in its value occurring downstream of incipient separation point after which it decreases abruptly in the back-flow region. Here the *rms* value is non-dimensionalized by the local mean wall static pressure in order to reduce the effect of mean flow properties. Such a trend appeared in all the *rms* distributions at different NPR suggesting that the large amplitude pressure fluctuations were triggered by the same mechanism. The difference mainly, however, lies in the peak *rms* intensity which varies with different operating conditions (and is discussed later). The plot also shows significant discrepancy in *rms* value (approximately by 80%) at circumferentially opposite intermittent separation locations. Such large variations in pressure fluctuations along the circumferential direction can, during transient operations, result in the generation of lateral forces.

3.3.2 Random pressure pulsation of a tilted separation shock

The time-history of wall pressure signal for NPR=28.9 from transducers located at the 5th, 6th and 7th streamwise pressure points for $\varphi = 0^{\circ}$ and 180° (circumferentially opposite) show some interesting features, Figure 10 (a)-(c) and (d)-(f), respectively. At $X/r_t = 8.04$ ($\varphi = 0^{\circ}$) the signal shows a highly intermittent nature and is seen to jump between two levels namely, a lower level indicating undisturbed boundary-layer condition (P_{w1}) and a higher level indicating shock passages (P_{w2}) in Figure 10 (b). P_{w1} is pressure signal measured when the "foot" of the separation shock moves downstream of this transducer, whereas P_{w2} is measured when the separation shock moves upstream of this transducer. No such behavior is indicated by the wall pressure signal from $\varphi = 180^{\circ}$, Figure 10 (e). The behavior of all other wall pressure signals from circumferentially opposite transducer locations (but placed at similar streamwise locations) also suggests that the separation front is tilted even when the NPR is held constant. The time-history of wall pressure signals (from the above three transducer locations) as the NPR of 28.9 is approached, Figure 11, shows that the separation front reaches the transducer locations at circumferentially opposite locations at different time instants indicating considerable flow asymmetry. Such an asymmetric transient phenomena can strongly contribute towards the generation of side-loads in nozzles.

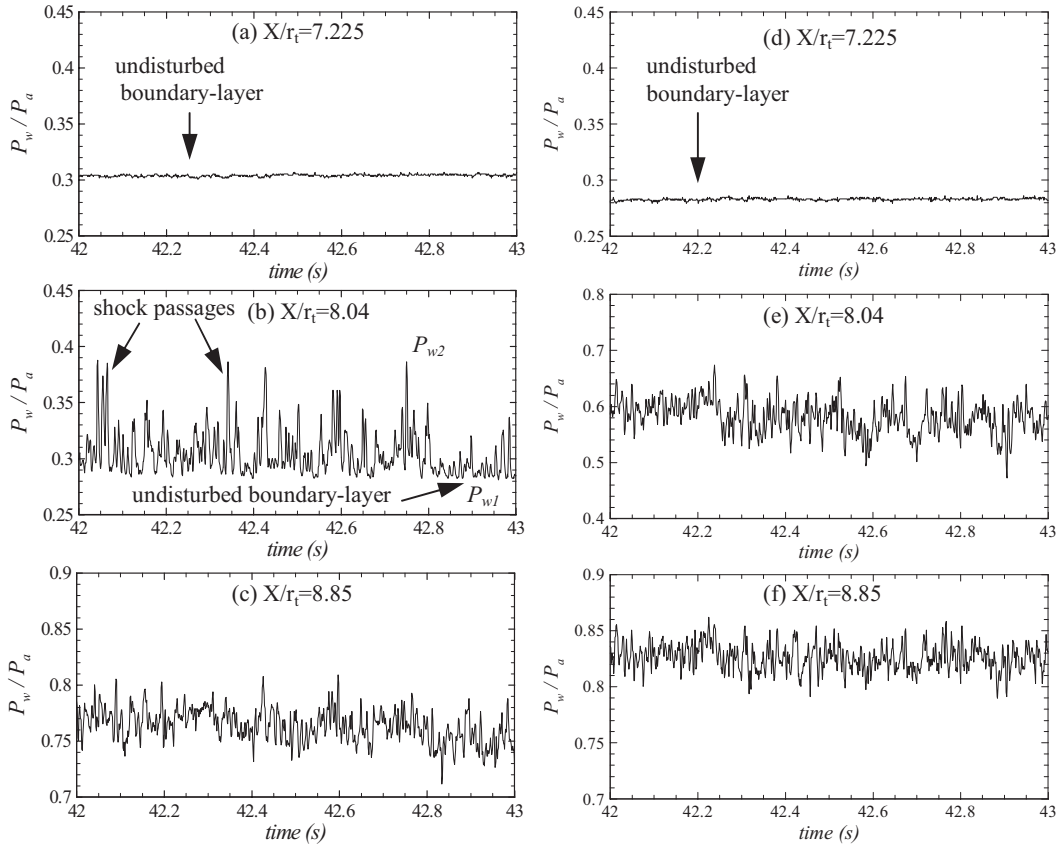

Figure 10. Time-history of wall pressure signal for transducer locations showing movement of separation shock: (a)-(c) φ = 0deg. and, (d)-(f) φ = 180deg: NPR=28.9

An immediate outcome of flow asymmetry in a round nozzle is a tilted physical separation front along the nozzle circumference. One such case was observed at NPR=39.8 using surface oil visualization, Figure 12 (a). For this NPR the separation region (containing the incipient, intermittent and physical separation information) was captured by the circumferentially placed transducers at the 11th and 12th locations. The 11th pressure point location ($X/r_t = 12.04$) for this NPR is the incipient separation location, Figure 8 (a), whereas the 12th pressure point locations ($X/r_t = 12.835$) lie partially in the separation region and partially in the back-flow region immediately downstream of the physical separation location ($X/r_t = 12.54$), Figure 12 (a). Transducers at locations 12 and 12A are seen to be upstream of the physical separation line while 12B lies on the separation line and 12C and 12D lie

immediately downstream of separation line. The circumferential *rms* distribution for the incipient separation locations shows considerable variation in its value, Figure 12 (b) suggesting significant asymmetry in shock unsteadiness characteristics.

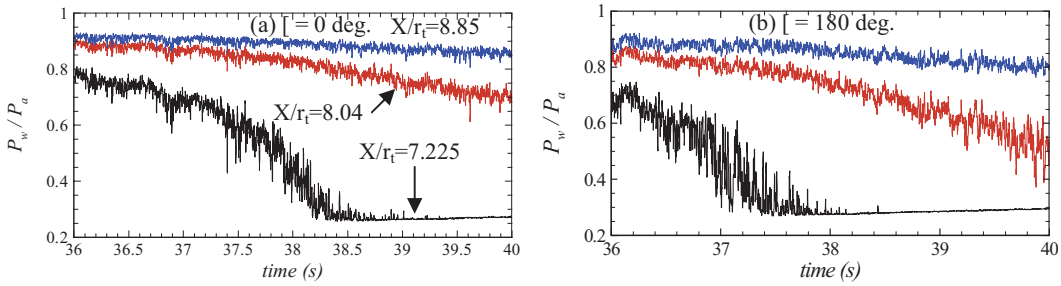

Figure 11. Time-history of wall pressure signals from pressure sensors placed at (a) φ = 0 deg. and (b) φ =180 deg. showing the difference in time of arrival of separation front as NPR=28.9 is reached

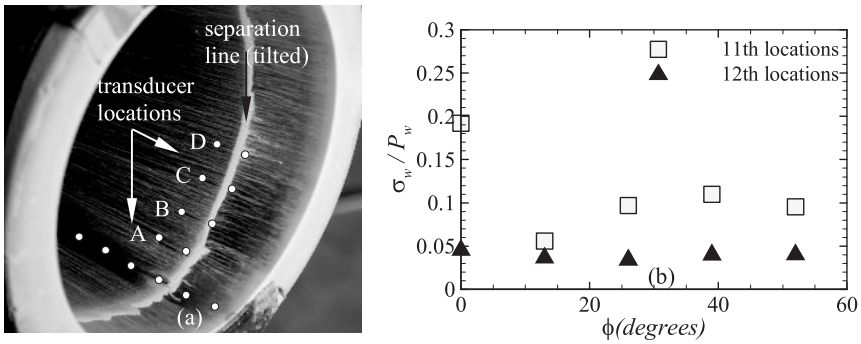

Figure 12. Variation of (a) physical separation line along the nozzle circumference and, (b) the corresponding rms distribution for 11th and 12th location transducers

Figure 13 shows the power spectral density of the wall pressure signals in the interaction region since the wall pressure signals for these circumferentially placed transducers at 11th and 12th locations were acquired at 25kHz. Here *G(f)* is plotted against frequency *f* on a linear-log scale in order to highlight the dominant frequencies in the signal. The wall pressure signal from incipient separation location/point of maximum *rms* for $\varphi = 0^{\circ}$ is dominated by high-amplitude lowfrequency fluctuations between 40Hz-400Hz, Figure 13 (a). However, for $\varphi = 13^{\circ}$, a large fraction of the energy is seen for frequencies less than 100Hz. Once again for $\varphi = 260$ and 390, Figure 13 (b)-(c), the fluctuations appear for frequencies below 500Hz but with considerably low amplitudes. In the separated region, on the other hand, the spectra show large fraction of the energy/fluctuations spread in 200-1000Hz frequency range with a dominant peak at 800Hz for all circumferential locations, Figure 13 (e)-(h). This suggests that in the separated region the pressure fluctuations caused by the turbulent structures in the separated shear layer contribute towards relatively higher frequencies > 500Hz. A significant variation in the spectra is exhibited for the incipient separation location circumferentially although not much can be seen for the transducers in the separated region. This suggests circumferential variation in the point of maximum *rms* location.

A possible physical mechanism responsible for generation of flow unsteadiness during such a free shock separation (FSS) condition seems to be the back-flow region that is set into pressure pulsations (caused by the aspiration effect of the turbulent structures in the separated jet being convected downstream) due to the close proximity of turbulent shear-layer, emanating from the separation point, to the nozzle wall [22]. This can cause asymmetric pressure distribution in the back-flow region along the nozzle circumference and hence, influence the local position of the separation front through the subsonic re-circulation region. This in turn is a strong function of NPR, as discussed earlier and the radial size of the recirculation zone defined by $(\epsilon_e - \epsilon_{sep})$.

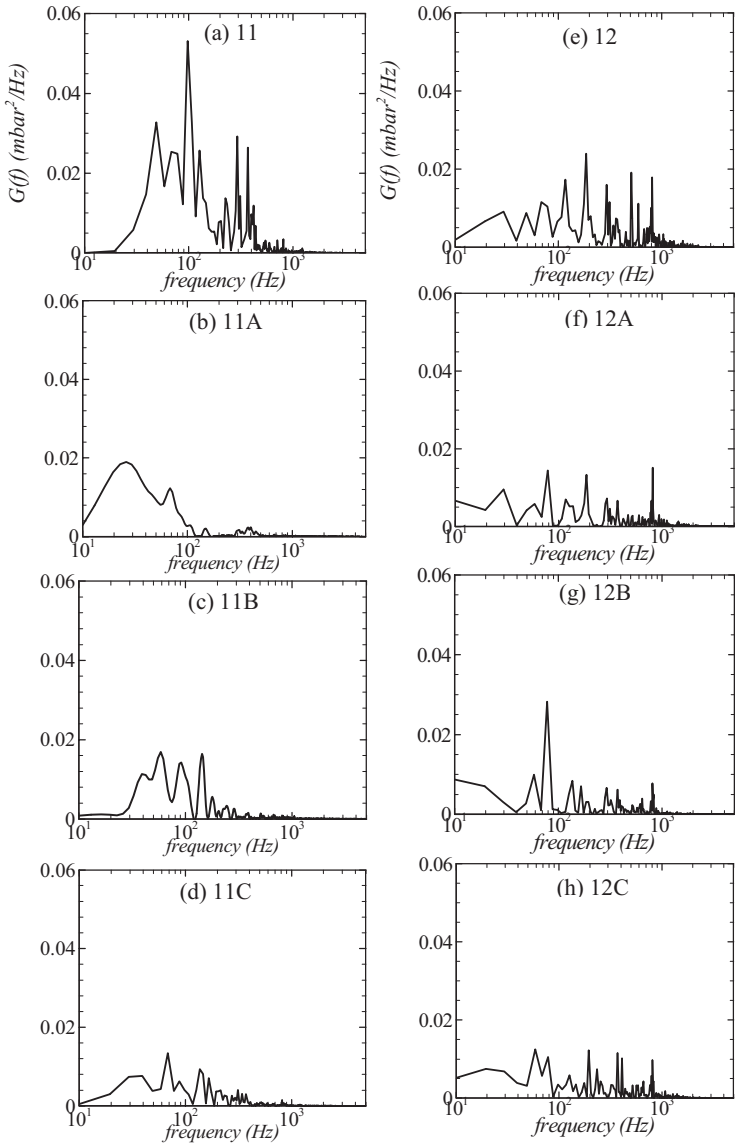

Figure 13. Circumferential evolution of power spectra for wall pressure signals from 11th and 12th wall pressure transducers; NPR= 39.8

Lawrence and Weynand [5] observed from a large number of test cases that the wall pressure just downstream of separation strongly influences the separation pressure and hence, the position of separation. It is however not clearly understood as to what extent the pulsations in the back-flow region affect the separation shock fluctuation. A preliminary examination of the wall pressure signal and its associated power spectra from separation and separated regions was carried out for NPR=28.9. It can be seen that for both φ=0˚ and 180, the traces of pressure fluctuations felt in the intermittent/separation regions are also felt in the back-flow/separated regions, 14 (a) and (c). The power spectra of these signals show low-amplitude low-frequency fluctuations with a dominant frequency centered around 24Hz and 100Hz that shows a subsequent drop in amplitude as the distance in the back-flow region progresses downstream, Figure 14 (b) and (d). This strongly suggests that there is a strong influence of pressure fluctuations in the back-flow region on the separation shock unsteadiness. As the length of the back-flow region decreases (i.e., as the separation front reaches closer to the nozzle-exit into the end-effect regime), this influence seems to die down with the power spectra showing no traces of separation shock unsteadiness in the back-flow region. In general it can therefore be said that the pulsations of the separation shock are perhaps dependent on the length of back-flow region, the strength of the separation shock and the local wall contour experiencing the flow separation. This may directly affect the length

of separation region which in turn can affect the *rms* distribution circumferentially. However a more detailed study with high frequency data acquisition for all streamwise located transducers needs to be carried out to confirm the influence of back-flow fluctuations on the separation shock unsteadiness, especially for NPR < 40.

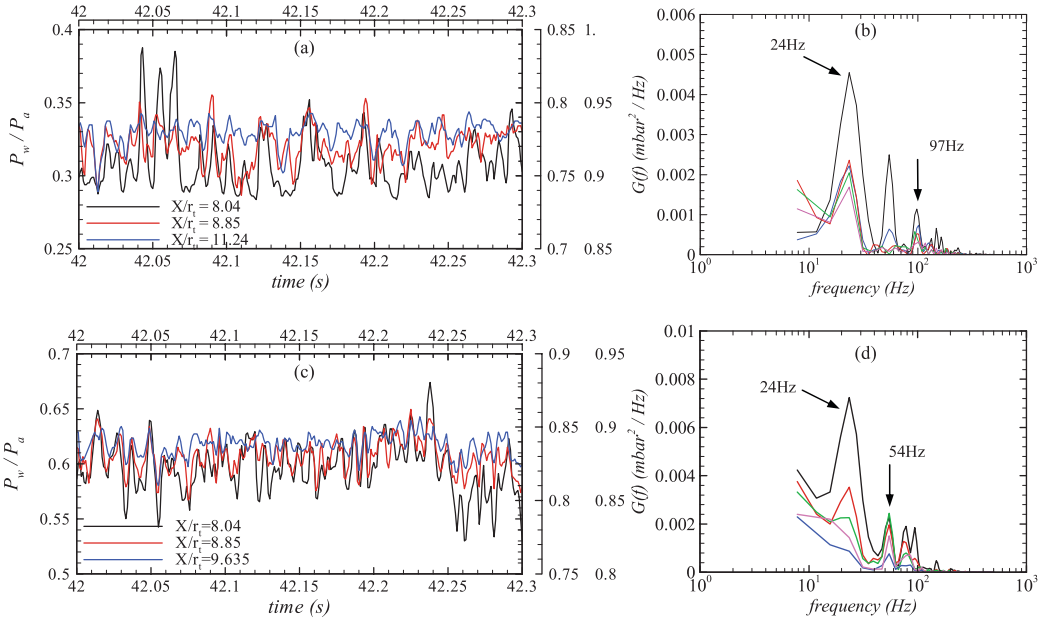

Figure 14. Influence of back-flow fluctuations on the shock unsteadiness in the separation region for (a) wall pressure signals at φ=0, (b) power spectra for wall pressure signals at φ=0, (c) wall pressure signals at φ=180, (d) power spectra for wall pressure signals at φ=180 and ; NPR=28.9

3.3.3 Variation in the length of separation region

The strongest contributor towards the origin of side-loads therefore seems to be therefore the random pressure pulsation of the separation shock in the separation region (between X_{inc} and X_{sep}). This region not only experiences the movement of separation shock but also experiences a sudden increase in P_w from very low values to approximately 60-70% of ambient pressure. An attempt was therefore made to study the effect of the variation in the length of separation region on sideload contribution.

Initially the maximum '*rms*' values (as indicated by the peak in '*rms*' value in Figure 9 (b)) from independent test runs were plotted against its corresponding NPR for both start up and shut down sequences and for transducer locations along $\varphi = 0^\circ$, Figure 15, as suggested by Verma *et al* [12]. No data was possible for NPR < 15. It can be observed that the $(\sigma_w/P_w)_{max}$ value shows distinct rise and fall in its value as the NPR is increased and decreased. The $(\sigma_w/P_w)_{max}$ value for start up case shows three peaks occurring at NPR=25, 30 and 40, after which the $(\sigma_w/P_w)_{max}$ value begins to drop significantly (end-effect regime) and tends to remain more or less constant. For the present case the magnitude of these peaks is much lower than that reported by Verma *et al* [12] for a TOP nozzle.

The $(\sigma_w/P_w)_{max}$ values for $\varphi = 180^\circ$ are also plotted in Figure 15 for comparison. It can be seen that a considerable discrepancy in $(\sigma_w/P_w)_{max}$ values exist for the two circumferentially opposite locations. This suggests that the flow is dominated by flow asymmetry at most NPR values below 45. The strongest cause of lateral-force origin in a TIC nozzle therefore seems to be the asymmetry in separation front around the nozzle circumference. This asymmetry causes variations in the pressure rise at separation and hence, in the local value of $(\sigma_w/P_w)_{max}$ (which is sensitive to the extent of separation region). Figure 16 (a) shows the variation in incipient separation and physical separation locations while Figure 16 (b) shows the variation in the length of separation or $(X_{sep} - X_{inc})/r_t$ as a function of NPR for start-up operation. It is interesting to point out that during start-up operation the length of separation region shows considerable variations and tends to peak at approximately similar NPR as those at which peaks in $(\sigma_w/P_w)_{max}$ value and strain-gauge signal are observed, Figure 17. Similar

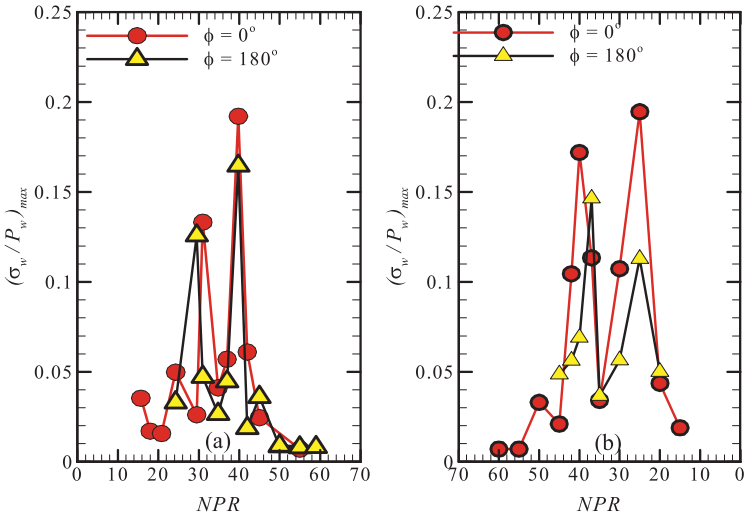

Figure 15. Variation of maximum rms in the region of flow separation as a function of NPR during (a) start up and, (b) shut down sequences, respectively.

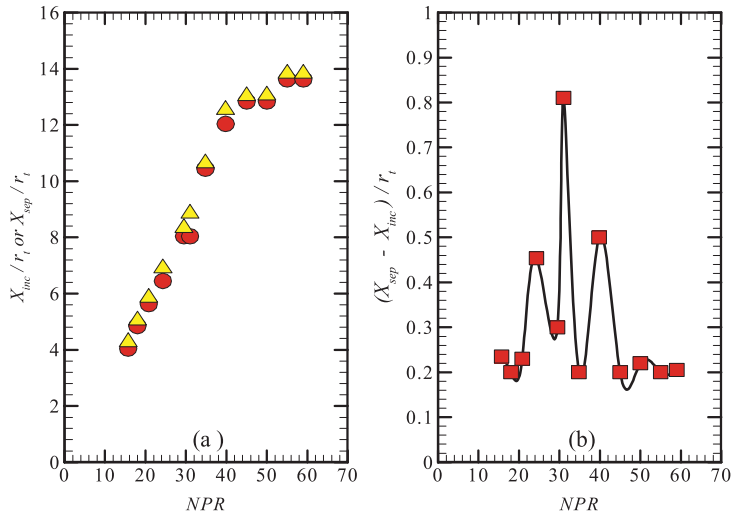

Figure 16. Variation of (a) incipient separation and physical separation location and, (b) (X_{sep} - X_{inc})/r_t as a function of NPR for start-up operation, respectively.

results have recently been reported by Verma and Haidn [21] for a TOP nozzle where the length of separation region is seen to peak as a flow transition NPR is approached each time. The accuracy of this study however is limited by the pitch of transducer locations in streamwise direction and therefore needs further scrutiny.

An asymmetry in separation front alone however cannot be responsible for the generation of flow unsteadiness and hence, towards the origin of lateral-forces. This point was further scrutinized for a case where an asymmetry in the separation front was observed for NPR 58 (oil picture not shown). But interestingly the strain-gauge signal did not show any increase in its magnitude, Figure 16. *This means that an important condition for side-load generation is not just flow asymmetry but also the length of separation region which begins to decrease as the separation front approaches closer to the nozzle exit (end-effect regime) with a subsequent reduction in wall pressure fluctuations*.

3.3.4 Flow transitions

Flow transitions in nozzles, especially those observed in thrust optimized parabolic (TOP) nozzle are known to result in peaks in the side-load signal [12-13, 16, 21-22]. Although no such flow transitions are known to be prevalent in this type of nozzle due to the type of Mach reflection that exists, the one

that exists at low NPR is common in both these nozzles. This was initially named as quasi-restricted shock separation (qRSS) and has been extensively studied by Stark et al. [36].

Figure 17 shows the time-history of strain gauge signal in the X-Z plane of the nozzle during a test run. The strain gauge signals shows two distinct peaks corresponding to qRSS at low NPR (approximately at 4 & 8) and one at high NPR of 40. In between these NPR the strain gauge signal shows an increase in the magnitude of strain-gauge signal but with no prominent peaks. Beyond NPR 40, the signal shows a significant decrease in magnitude and marks the beginning of end-effect regime.

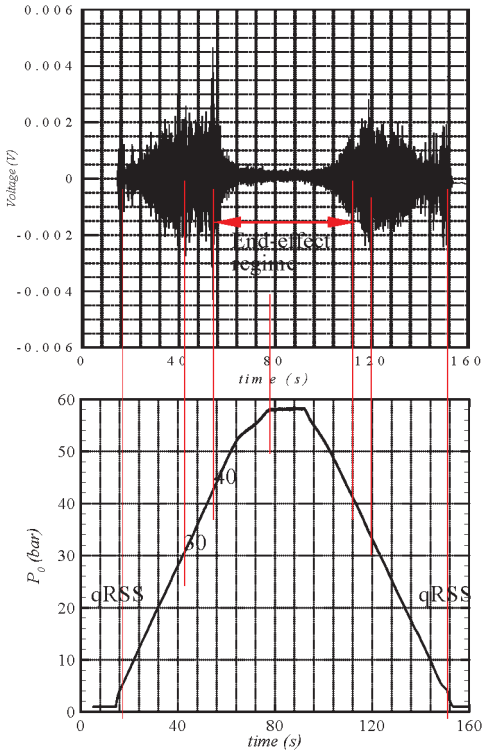

Figure 17. Variation of (a) voltage signals from the strain gauges installed on the bending tube along XZ plane and, (b) corresponding stagnation pressure variation with time.

3.4 Physical causes of separation shock unsteadiness in nozzles

It is interesting to discuss possible causes that lead to side-load origin in nozzle flows. Shockwave boundary-layer interactions on swept compression corners have shown that the overall *rms* levels in the interaction as well as the maximum *rms* levels generated by the translating separation shock increase with decreasing sweep and *vice-versa*. Further the length of the intermittent region, over which the separation shock foot translates increases with decreasing sweep. These correlate well with our finding in nozzle flows. The role of shock strength variation also needs to be investigated in triggering the large-scale motion of separation shock and hence, in the overall flow unsteadiness.

Past studies indicate that the separation shock unsteadiness can be caused by two different physical phenomena. The small-scale or jittery motion is caused by fluctuations in the ratio of static quantities across the shock foot. These perturbations induce fluctuations in the separation shock velocity and thus changes in separation shock position are an integral result of the velocity fluctuations. The large-scale or global motion of the separation shock on the other hand is caused by a displacement mechanism related to the dynamics of the separated flow. Thus, an expansion of the separated flow, for example, displaces the separation shock to an upstream position, whereas a contraction of the separated flow results in a displacement in the downstream direction. In nozzle flows with the absence of a separation bubble as during FSS condition, the large-scale motion could be triggered due the interaction between the separated jet and the accelerating flow into the nozzle in the back-flow region. As the length of back-flow region decreases, the separation shock oscillations begin to die down and hence the side-load signal drops even when the separation front exhibits circumferential asymmetry.

3.5 Flow Separation Criteria

Separation criteria have been developed in the past from the experimental data to serve as a prediction tool for the separation point. However an accurate prediction has always been difficult due to a lot of parameters involved in the shock-wave boundary-layer interaction phenomena occurring in nozzles such as nozzle contour, gas properties, wall roughness, wall temperature etc. Figure 18 shows a comparison of some of these criteria with the experimental data from hot and present cold flow tests. Significant scatter is apparent between the hot and cold tests. Although Schmucker's criteria is widely accepted with an additional margin of 20% from the predicted separation occurrence (as per NASA's recommendation in 1976), Hagemann's criteria [37] agrees very well with the hot-test data while Ostlund criteria [37] data agrees very well with the conical nozzles and present cold flow tests. These latter criteria are based on the linear dependence of the Mach number on both the deflection angle θ and the shock angle β [37]. Another approach towards prediction of separation pressure ratio is suggested by Reshotko and Tucker [38] and Lawrence and Weynand [5] who derived an equation resulting in Mach number ratio (M_2/M_{inc}) across the separation region. Figure 18 (b) shows a comparison plot of Lawrence and Weynand [5] criteria with experimental data. It can be seen that the present curve fit ($M_2 = 0.695M_{inc}+0.1975$) fits well with most of the plotted experimental data and is close to that suggested by Reshotko and Tucker [38] ($M_2/M_{inc} = 0.762$). The criteria of Lawrence and Weynand ($M_2/M_{inc} =0.8$) is good for conical nozzles with nozzle half divergence angle > 15 but does not agree well for contoured nozzles [5].

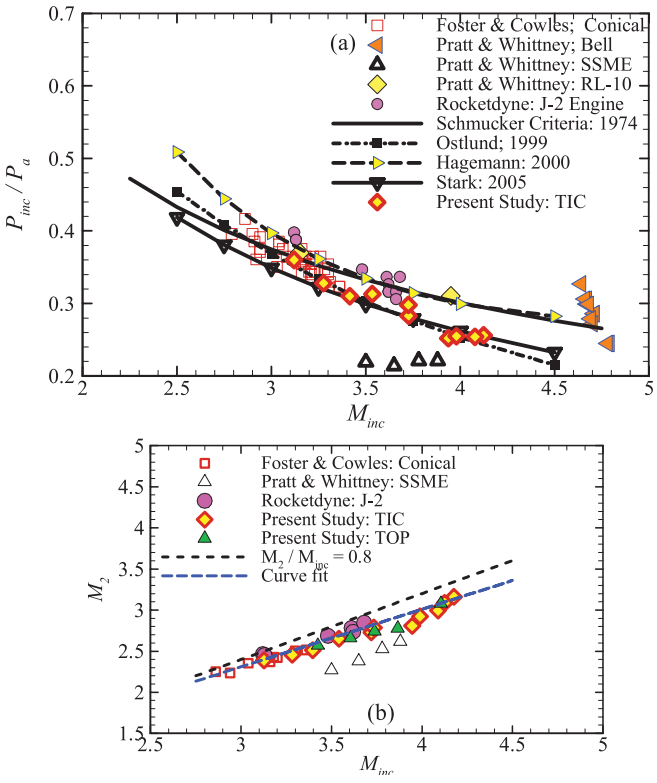

Figure 18. Comparison of the present cold test start up data for TIC and TOP nozzles with previous hot tests for (a) the pressure rise P_{inc}/P_a as a function of separation Mach number (b) Mach number ratio across the separation shock

4.0 CONCLUSIONS

This paper discusses the exhaust flow features and the unsteady flow separation characteristics of overexpanded subscale rocket nozzles. A D_iMR type of Mach reflection features in the TIC nozzle while an I_nMR is seen in a TOP nozzle. The main contributor towards generation of sideload signal in a TOP nozzle is known to be the flow transition from FSS-RSS and vice-versa and the shock unsteadiness preceding them. But in a TIC nozzle where only FSS condition exists, the strongest causes

of lateral force origin are seen to be (i) the asymmetry of separation front around the nozzle circumference, (ii) length of separation region and, (iii) length of back-flow region. The asymmetry of separation front is seen to cause variations in the pressure rise at separation and hence, in the local value of $(\sigma_w/P_w)_{max}$. The length of separation region also shows considerable variations with NPR and tends to peak at NPR similar to those at which peaks in $(\sigma_w/P_w)_{max}$ value and strain-gauge signal occur. Data therefore suggests that that the important condition for side-load generation is not just flow asymmetry but also the length of separation region which begins to decrease as the separation front approaches closer to the nozzle exit with a subsequent reduction in wall pressure fluctuations. The small-scale or jittery motion seems to be caused by fluctuations in the ratio of static quantities across the shock foot while the large-scale motion could be triggered due the interaction between the separated jet and the accelerating flow into the nozzle in the back-flow region. As the length of back-flow region decreases, the separation shock oscillations begin to die down and hence the side-load signal drops even when the separation front exhibits circumferential asymmetry.

ACKNOWLEDGEMENTS

The results reported in this paper are from the work carried out by the first author during his tenure as a research scientist in the Nozzle flow Group at Space Propulsion Institute, DLR Lampoldshausen, Germany between May 2001 to December 2003. The authors would like to thank Ralf Stark, H.K.Ciezki, H. Kronmueller and Christian Boehm for their help during the entire course of the test campaigns.

REFERENCES

[1] Foster, C. and Cowles, F., "Experimental Study of Gas Flow Separation in Overexpanded Exhaust Nozzles for Rocket Motors", *JPL Progress Report 4-103*, May 1949.

[2] Summerfield, M., Foster, C., and Swan, W., "Flow separation in overexpanded supersonic exhaust nozzles. *Jet Propulsion*, 24(9), 319-321(1954)

[3] Arens and Spiegler, "Shock Induced Boundary-Layer Separation in Overexpanded Conical Exhaust Nozzles", *AIAA Journal*, Vol.1, No.3, March 1963, pp. 578-581.

[4] Schmucker, R., "Flow Processes in Overexpanding Nozzles of Chemical Rocket Engines", (in German), Report TB-7,-10,-14, Technical University Munich.

[5] Lawerence, R.A. and Weynand, E.E., "Factors Affecting Flow Separation in Contoured Supersonic Nozzles", *AIAA Journal*, Vol.6, No.6, 1968, pp.1159-1160

[6] Sutton, George, P. and Biblarz, O., Rocket Propulsion Elements, Seventh Edition, John Wiley & Sons, Inc

[7] Dumnov, D., "Unsteady side-load acting on the nozzle with developed separation zone", AIAA 96-3220

[8] Nave, L.H. and Coffey, G.A., "Sea level side-loads in high area-ratio rocket engines", AIAA Paper 73-1284

[9] Oestlund, J., Damgaard, T. and Frey, M., "Side-load phenomena in highly overexpanded rocket nozzles", *Journal of Propulsion and Power*, 20 (4), 695-704 (2004)

[10] Terhardt, M., Hagemann, G. and Frey, M., "Flow separation and side-load behavior in the Vulcain engine", AIAA 99-2762.

[11] Frey, M. and Hagemann,G., "Flow separation and side-loads in rocket nozzles", AIAA-99-2815

[12] Frey, M. and Hagemann, G, "Restricted shock separation in rocket nozzles", *Journal of Propulsion and Power*, 16(3), 478-484 (2000)

[13] Hagemann, G., Frey, M. and Koeschel, W., "Appearance of restricted shock separation in rocket nozzles", *Journal of Propulsion and Power*, 18 (3), 577-584 (2002)

[14] Onofri M., and Nasuti, F., "The physical origins of side-loads in rocket nozzles", AIAA 99-2587.

[15] Nasuti,F. and Onofri, M., " Viscous and Insicid Vortex generation During Start up of Rocket Nozzles", *AIAA Journal*, 1998, Vol 36, No.5, pp 809-815.

[16] Frey, M., Stark, R., Ciezki, H.K., Quessard, F., and Kwan, W., "Subscale nozzle testing at the P6.2 test stand", AIAA 2000-3777

[17] Watanabe, Y., Sakazume, N., and Tsuboi, M.: LE-7A Engine nozzle problems during the transient operations. AIAA 2002-3841

[18] Watanabe, Y., Sakazume, N., and Tsuboi, M.: LE-7A engine separation phenomenon differences of the two nozzle configurations. AIAA 2003-4763.

[19] Nguyen, A.T, Deniau, H., Girard, S. and Alizary de Roquefort, T: Wall Pressure Fluctuations in an Overexpanded Rocket Nozzle. AIAA 2002-4001

[20] Verma, S.B., Stark, R. and Haidn, O., "Relation between shock unsteadiness and the origin of side-loads in a thrust optimized parabolic rocket nozzle. *The Aerospace Science and Technology Journal*, 10(6), August 2006

[21] Verma, S.B. and Haidn, O., "Surface Flow Studies of Restricted Shock Separation in a Thrust Optimized Parabolic Nozzle'', *Journal of Shock Waves*, Detonations and Explosions, DOI 10.1007/s00193-009-0211-0

[22] Verma, S.B., "Shock Unsteadiness in a Thrust Optimized Parabolic Nozzle'', *Journal of Shock Waves, Detonations and Explosions, Special issue on Nozzle Flow Separation*, Volume 19, Issue 3 (2009), Page 193

[23] Verma, S.B., "Study of Flow Separation in a Truncated Ideal Contour (TIC) Nozzle", *AIAA Journal of Propulsion and Power*, September-October, Vol. 18, No. 5, 2002, pp. 1112-1121.

[24] Frey, M. and Hagemann, G.: Status of Flow Separation Prediction in Rocket Nozzles. AIAA Paper No-98-3619

[25] Courant, R. and Freidrichs, K.O.(1948), Hypersonic Flow and Shock Waves, Wiley Interscience, New York.

[26] Ben Dor, G., Igra, O. and Elperin, T., *Handbook of Shock Waves, Vol. 2 Shock Wave Interactions and Propagation*, Academic Press, 2001.

[27] Henderson, L.F. and Lozzi, A., "Experiments on Transition of Mach Reflections'', *Journal of Fluid Mechanics*, 1975, Vol. 94, pp. 541-559.

[28] Frey, M. "Shock Patterns in the Exhaust Plume of Rocket Nozzles", *Proceedings of the 3rd European Symposium on Aerothermodynamics of Space Vehicles*, pages 395—403, ESAESTEC, Noordwijk, The Netherlands, 1998.

[29] Stark, R. and Wagner, B., "Experimental study of boundary layer separation in truncated ideal contour nozzles'', Journal of Shock Waves, 2009, Vol. 19, Issue 3, pp 185–191

[30] Verma, S.B. and Haidn, O., "Studies on Restricted Shock Separation in a Thrust Optimized Parabolic Nozzle," AIAA Journal of Propulsion and Power, 2009, Vol. , No., pp. 17

[31] Okada, Y., Sunouchi, K., Ryu, H., Patra, A., Ashmine, K. And Takeuchi, K, "Measurement of Condensation Onset in Steady Supersonic Laval Nozzle Flow for the Molecular Laser Isotope Separation Process'', *Journal of Nuclear Science and Technology*, 1998, Vol. 35, No. 2, pp. 158-162.

[32] Doeffer, P., Szumowski, A. and Yu, S, "The effect of Air Humidity on Shock Wave Induced Incipient Separation'', *Journal of Thermal Science*, 2000, Vol. 9, No.1, pp. 45-50

[33] Setoguchi, T. and Matsuo, S., "Effect of Non-Equilibrium Homogenous Condensation on Flow Fields in a Supersonic Nozzle'', *Journal of Thermal Science*, 1996, Vol. 6, No.2, pp. 90-96

[34] Dolling, D.S. and Narlo II, N.C., "Driving Mechanism of Unsteady Separation Shock Motion in Hypersonic Interactive Flow'', *AGARD-CP-428, Aerodynamics of Hypersonic Lifting Vehicles*, pp. 7-1 to 7-12, 1987.

[35] Muck, K.C., Andreopoulos, J. and Dussauge, J.P.: Unsteady nature of shock-wave/turbulent boundary-layer interaction. *AIAA Journal*, 26 (2), 179-187 (1988)

[36] Kwan, W and Stark, R., "Flow Separation Phenomena in Subscale Rocket Nozzles'', AIAA-2002-4229

[37] Östlund, J." Flow Processes in Rocket Engine Nozzles with Focus on Flow Separation and Side-Loads'', TRITA-MEK, Technical Report 2002:09, ISSN 0348-467X.

[38] Reshotko, E. and Tucker, M., "Effect of Discontinuity on Turbulent Boundary-Layer Thickness Parameters and Application to Shock-Induced Separation'', NACA TN-3454, May 1955.